ACS Catalysis

pubs.acs.org/acscatalysis

Research Article

Highly Selective Cross-Etherification of 5-Hydroxymethylfurfural with Ethanol

Meredith C. Allen,[⊥] Alexander J. Hoffman,[⊥] Tsung-wei Liu, Matthew S. Webber, David Hibbitts,* and Thomas J. Schwartz*

Cite This: *ACS Catal.* 2020, 10, 6771−6785

Read Online

ACCESS | Metrics & More | Article Recommendations | Supporting Information

ABSTRACT: Etherification of 5-hydroxymethylfurfural (HMF) and ethanol to yield ethoxymethylfurfural (EMF) is an important reaction for producing diesel blendstocks from biomass resources. This aqueous-phase etherification reaction occurs with higher selectivity on H-BEA (95%) than on Amberlyst-15 (76%), H-FAU (64%), H-MFI (88%), and H-MOR (63%) at high conversions (>60%). This selectivity toward EMF is not driven by transport limitations or Brønsted acid site concentrations; instead, a kinetic preference for etherification on BEA leads to such high yields. Nonidealities associated with the liquid-phase reaction are addressed by using UNIFAC-derived activities rather than concentrations, and reaction kinetics measurements indicate that the reaction proceeds on a surface saturated by ethanol with rates that are first order with respect to HMF activity and negative order with respect to ethanol activity. Gas-phase density functional theory calculations are unified with aqueous liquid-phase kinetics measurements by using partial pressures of a hypothetical gas phase calculated from UNIFAC-derived activities. DFT calculations indicate that etherification occurs in a single concerted step—rather than through a two-step sequential pathway—in which HMF is protonated and dehydrated to form a relatively stable methoxyfurfural carbocation (in contrast to ethanol dehydration). This methoxyfurfural carbocation is stabilized by resonance in contrast to ethyl carbocations formed from ethanol protonation and dehydration, and it also leads to the observed high selectivity for cross-etherification (to EMF) vs self-etherification of either HMF or ethanol. This rigorous mechanistic investigation uses gas-phase DFT calculations to offer insights into aqueous-phase catalysis, thereby elucidating an important reaction in biomass upgrading.

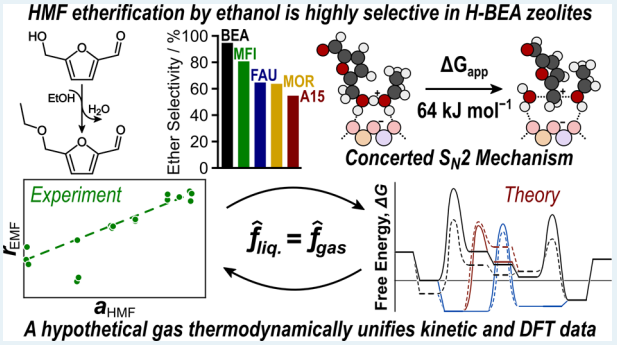

KEYWORDS: *zeolite catalysis, etherification, 5-hydroxymethylfurfural, biomass conversion, biobased chemicals*

1. INTRODUCTION

Lignocellulosic biomass is a renewable carbon resource that is attractive for its potential to replace fossil-based resources,[1,2] a need which has been exacerbated in the United States by the predominance of light hydrocarbon feedstocks that are poor precursors to chemicals requiring five or more carbon atoms.[3−6] The use of platform chemicals provides a flexible approach for producing a variety of valuable products from a handful of common intermediates.[4] One such platform molecule is 5-hydroxymethylfurfural (HMF), which can be produced in high yields from C_6 sugars[7−16] and has been upgraded via a large number of processes to both fuels and chemicals.[17,18]

The etherification of HMF (Scheme 1) is an important reaction that has been studied as a means of producing ethoxymethylfurfural (EMF), which is suitable for direct blending with diesel fuel.[19−21] Solid Brønsted acids catalyze the formation of EMF from HMF, including Amberlyst-15,[20,22] Amberlyst-131,[23] and Al-MCM-41.[22] H-BEA has also been used for HMF etherification to produce not only EMF[24] but also 5-*tert*-butoxymethylfurfural (by reacting HMF with *tert*-butanol)[25] and surfactants (by reacting HMF with long-chain alcohols).[26] These etherification reactions have also been performed in one pot starting from glucose using a combination of Sn-containing BEA zeolite and HCl,[15,23]

Scheme 1. Etherification of HMF with Ethanol

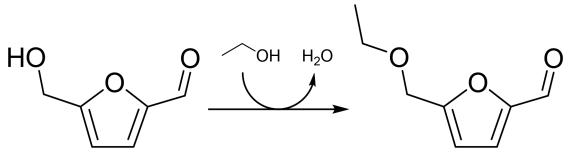

Received: March 22, 2020
Revised: May 5, 2020
Published: May 11, 2020

https://dx.doi.org/10.1021/acscatal.0c01328
ACS Catal. 2020, 10, 6771−6785

while 2,5-diethoxymethylfuran can be produced by coupling transfer hydrogenation with etherification over Hf-, Zr-, and Sn-BEA zeolites.[27,28] While etherification can be performed solely over Lewis acid sites (e.g., Zr/SBA-15[22] and NH_4^+ BEA zeolite[24,29]), such studies have not generally been performed in the presence of water. Recent *in situ* and *operando* spectroscopy measurements have indicated that these Lewis acid sites form pyridinium ions in aqueous solution upon titration with pyridine, suggesting that they function as Brønsted acid sites in the presence of water.[30,31] Such considerations are important for reactions with HMF because any practical application of HMF etherification to produce biodiesel, surfactants, or other chemicals must contend with the ubiquity of water in biomass processing.

Etherification reactions generally follow an S_N2-type pathway with a concerted (or associative) transition state.[32] Previous work by Bell and co-workers[33,34] assumed this pathway dominates over tungstated zirconia for the conversion of various long-chain alkanols to their corresponding mixed ethers. Importantly, the activation energies for these various self- and cross-etherification reactions are comparable, indicating poor selectivities to a single cross-etherification product.[34] Along the same lines, spectroscopic and computational studies using a variety of Brønsted acid catalysts show similar results for both methanol[35] and ethanol[36] dehydration to dimethyl and diethyl ethers, and a bimolecular transition state is formed during diethyl ether formation over Lewis acid sites on γ-Al_2O_3.[37] In contrast, for HMF etherification, Balakrishnan et al. postulate a reaction mechanism wherein the furan is protonated and undergoes dehydration in a rate-limiting step. The resulting oxocarbenium ion then undergoes nucleophilic attack by ethanol to yield the ether in a two-step (sequential or dissociative) mechanism.[19]

In this work, we demonstrate that H-form BEA zeolite catalysts provide exceptional cross-etherification selectivities (>90%) to EMF at high conversions (>60%), thereby avoiding self-condensation of either ethanol or HMF. We then use a combination of reaction kinetics measurements and density functional theory (DFT) calculations to elucidate the mechanism by which ethanol reacts with HMF. Due to the practical concerns associated with performing biomass reactions in the absence of water, we have evaluated this mechanism in the presence of excess water. To compare our liquid-phase reaction kinetics data with calculations performed *in vacuo* using DFT, we develop a model based on a hypothetical gas phase that is in equilibrium with the experimental liquid phase. We find that the kinetics for these reactions are governed by transition states similar to those for previously investigated dehydration reactions of other alcohols. Finally, we show that a concerted bimolecular etherification mechanism prevails under the relevant experimental conditions.

2. MATERIALS AND METHODS

2.1. Catalyst Preparation. The zeolite catalysts were acquired from Zeolyst International. BEA zeolite was obtained with silica to alumina ratios (SiO_2:Al_2O_3) of 25 (ammonium form), 38 (ammonium form), and 300 (hydrogen form) (BEA-25, BEA-38, and BEA-300, respectively). MFI zeolite was obtained with SiO_2:Al_2O_3 = 23 (ammonium form), mordenite (MOR) with SiO_2:Al_2O_3 = 20 (ammonium form), and faujasite (FAU) with SiO_2:Al_2O_3 = 5.1 (ammonium form). Amorphous SiO_2−Al_2O_3 (ASA) with SiO_2:Al_2O_3 = 5.1 was acquired from Grace Davison (Davicat 3113). These catalysts were calcined in air (Matheson, breathing air) at 823 K for 1 h (ramp rate of 3 K min^{-1}). The calcined catalysts were crushed and sieved between 50 and 100 mesh. Amberlyst-15 (A15) in its hydrogen form (Sigma-Aldrich) was washed in Milli-Q grade water (18 MΩ) and dried overnight in an oven at 383 K. The washed A15 was also crushed and sieved between 50 and 100 mesh.

2.2. Reaction Kinetics Measurements. Reactions were performed in thick-walled glass batch reactors (Alltech, 10 mL) equipped with triangular stir bars and sealed with PTFE liners (Qorpac) in plastic caps (Qorpac). In a typical reaction, 4 mL of liquid feed containing 200 mM HMF (Acros Organics, 98%) and 12.9 M alcohol in aqueous solution was placed in a reactor containing the catalyst at an HMF to catalyst ratio of 10:7 (g:g). Alcohols used include ethanol (Acros Organics, 99.5+%), *n*-butanol (Sigma, ≥99.4%), phenol (Fisher, 91%), and cyclohexanol (Fisher, reagent grade). Reaction temperatures were maintained at 433 K in a stirred oil bath, and reaction times ranged from 15 min to 96 h to achieve the desired HMF conversions. Selectivity was measured at fractional conversions of HMF between 70 and 60%, and initial rates were measured at HMF fractional conversions below 15%. Reaction products were quantified using a Shimadzu GC-2010 instrument with an APC-2010 FID detector. Separation was achieved using an Agilent DB-634UI column (30 m × 0.025 mm, 1.40 μm). Helium (Matheson, grade 5.0) with a linear velocity of 35 cm s^{-1} was used as the carrier gas. Components were identified by comparison with retention times of known standards.

2.3. Catalyst Characterization. Diffuse reflectance infrared Fourier transform (DRIFT) spectra were recorded using a Nicolet 6700 Fourier transform infrared spectrometer (FTIR) equipped with a Praying Mantis (Harrick Scientific Production, IBC) accessory for DRIFT applications. KBr powder was placed in the sample cup inside a Harrick Scientific high-temperature reaction chamber (HVC). The sample cup in the HVC was placed on a temperature-controlled sample stage equipped with a cartridge heater and a thermocouple. The temperature of the sample cup was controlled by a Harrick Scientific automatic temperature controller (ATC-024-1).

KBr powder was placed into the sample cup and was heated under low vacuum (~3 Pa) at 473 K for several hours, after which a reference beam spectrum was recorded. Zeolite samples were spread on top of the KBr powder in the sample cup. Before pyridine adsorption, the samples were heated under vacuum for several hours at 473 K and a single-beam spectrum was recorded. Pyridine was introduced into the chamber at room temperature followed by 1 h of evacuation to remove gas-phase and weakly physisorbed pyridine. DRIFT spectra were recorded under evacuation by accumulation of 512 scans at 4 cm^{-1} resolution and using a mercury−cadmium−telluride (MCT) detector. After pyridine exposure, scans were measured at 293, 373, 423, and 473 K with 1 h of evacuation between each temperature. Difference spectra were obtained by subtracting the spectrum of the clean zeolite from the spectra obtained after pyridine adsorption.

In the pyridine difference spectra, peaks at 1545 cm^{-1} were assigned to pyridine bonded to Brønsted acid sites and peaks at 1455 cm^{-1} were attributed to pyridine bonded to Lewis acid sites.[38] Peak areas were measured by integrating linear-baseline-corrected curves from 1515 to 1565 cm^{-1} for the Brønsted acid peak and from 1435 to 1470 cm^{-1} for the Lewis

https://dx.doi.org/10.1021/acscatal.0c01328
ACS Catal. 2020, 10, 6771−6785

Table 1. Rates and Selectivity Data for Conversion of HMF to EMF Using Brønsted Acid Catalysts

catalyst	SiO_2:Al_2O_3	time, h	conv,[a] %	EMF sel, %	EL sel, %	Brønsted acid sites, μmol g^{-1}	initial EMF rate,[b] μmol g^{-1} s^{-1}	initial EMF TOF,[b] ks^{-1}
Amberlyst 15 (A15)	N/A	2.5	84	76	24	1800	1.69	0.94
faujasite (FAU)	5.1	48	88	64	nm[c]	678[d]	0.14	0.19
ZSM-5 (MFI)	23	24	66	88	7	1098[d]	0.22	0.20
mordenite (MOR)	20	5	73	63	nm[c]	1786[e]	0.36	0.21
beta zeolite (BEA-25)	25	2.5	66	95	<5	618[d]	1.65	2.7
beta zeolite (BEA-38)	38	1.5	73	90	<5	553[d]	1.62	2.9
beta zeolite (BEA-300)	300	4	60	91	<5	100[d]	0.25	2.6

[a]Reaction conditions: 4 mL of 200 mM HMF and 12.9 M C_2H_5OH in H_2O, HMF:cat. = 10:7 (g:g), 433 K. [b]Measured at HMF conversions below 15%, achieved by varying the contact time. [c]Not measured. [d]Measured by temperature-programmed desorption of isopropyl amine, reported by Semelsberger et al.[68] (FAU), Wan et al.[69] (MFI), Abdelrahman et al.[40] (BEA-25 and -38), and Luo et al.[28] (BEA-300) [e]Measured by temperature-programmed desorption of NH_3, reported by Hulea et al.,[70] coupled with the pyridine FTIR data in Table S1.

acid peak.[39] To correct for physisorbed pyridine, which appears in some samples as a shoulder on the Lewis acid peak,[38] two Lorentzians were fitted to the Lewis acid peak at 1455 cm^{-1} and the physisorbed pyridine peak at 1444 cm^{-1}. Analytical integrals for the Lorentzians were evaluated to calculate the fraction of the numerical area of the Lewis acid peak and to exclude the physisorbed pyridine peak. The ratio of the Brønsted area to the Lewis area was reported as the Brønsted/Lewis (B/L) absorbance ratio. To calculate the B/L concentration ratio, the absorbance ratio was corrected by molar extinction coefficients of pyridine on Brønsted and Lewis sites of 1.67 and 2.22 cm $\mu$$mol^{-1}$, respectively.[39]

The loading of Brønsted acid sites on each catalyst was obtained from a review of the literature. As has been shown recently by Dauenhauer's group,[40] the measurement of acid sites by temperature-programmed desorption of amines, as originally described by Gorte and co-workers,[41] is reproducible across many laboratories for commercial zeolite samples obtained from Zeolyst, Inc. Correspondingly, we have used these values for our analysis (individual citations given in Table 1).

2.4. Computational Details. Periodic, plane-wave density functional theory (DFT) calculations were performed using the Vienna ab initio simulation package (VASP)[42−45] implemented in a computational catalysis interface (CCI).[46] Plane waves were constructed using the projector augmented wave method (PAW)[47,48] with an energy cutoff of 400 eV. Structures were converged such that the forces on all atoms were <0.05 eV $Å^{-1}$, as determined by a fast Fourier transform (FFT) grid with a cutoff twice the plane-wave cutoff, and electronically converged to an energy difference between iterations of $<10^{-6}$ eV. The revised Perdew−Burke−Ernzerhof (RPBE) form of the generalized gradient approximation (GGA) was used to calculate electronic energies for all structures.[49] Dispersive interactions were included by adding the DFT-D3 dispersive correction with Becke−Johnson damping (D3BJ).[50] The Brillouin zone was sampled at the Γ point.

Transition state searches were initiated by nudged elastic band (NEB)[51,52] calculations with 16 images along the reaction coordinate and were converged such that forces on each atom were <0.3 eV $Å^{-1}$. From these calculations, transition states were refined using the dimer method,[53] which were converged such that the forces on all atoms were <0.05 eV $Å^{-1}$ and the energy difference between iterations was $<10^{-6}$ eV—the same convergence criteria used for optimization calculations.

The Si-form structure of the BEA zeolite was obtained from the International Zeolite Association (IZA) structure database with unit cell parameters $a = b = 12.632$ Å, $c = 26.186$ Å, and $\alpha = \beta = \gamma = 90.0°$.[54] BEA has straight 12-membered rings (12-MR) which connect and intersect to form a 2D pore network. The zeolite structure in which these calculations were performed resembles the polymorph A structure of BEA.[55,56] All calculations were performed at site T8 in the BEA structure,[55,56] which is surrounded by two symmetrically unique O atoms and is located at the intersection of the BEA 12-MRs. This site was chosen because of its proximity to the channel intersection within BEA, thus allowing for bimolecular reactions involving HMF, a relatively large molecule.

One challenge associated with the elucidation of reaction mechanisms for liquid-phase biomass conversion processes is that the bulk phase—a nonideal aqueous solution—is not readily modeled by density functional theory (DFT) calculations. Thus, even if one can model solvent molecules near the catalyst site (through explicit solvation, implicit solvation,[57,58] or a combination thereof), there is no straightforward means for unifying results from DFT and liquid-phase kinetics studies. This is especially relevant for reactions in zeolites, where the relative hydrophobicity of the zeolite micropores may reduce intrapore solvent aggregation, such that transition states are relatively "dry" while the bulk phase is "wet", complicating modeling efforts. Using an explicit or implicit solvent model around bulk molecules will influence their potential energies, but estimating the translational and rotational entropy of such molecules in the liquid environment is much more difficult and usually requires computationally intractable molecular dynamics simulations. Here, we overcome this challenge by modeling desorbed species as ideal gases and by unifying these ideal gases with the liquid phase through a hypothetical gas phase whose properties are dictated by vapor−liquid equilibrium (details in section 3.4). This thermodynamic manipulation is reminiscent of referencing proton energies to the standard hydrogen electrode when fuel cell chemistry at metal−water interfaces is modeled.[59]

Solvent molecules may also enter the BEA zeolite and congregate near Brønsted acid sites.[60,61] Here, we account for these solvent molecules using an implicit solvent model (VASPsol),[57,58] which allows us to tune the properties of that implicit solvent to qualitatively match the shifts in relative permittivity (from 80 to 15) that occur across the range of conditions studied in this work, in which the ratio of H_2O to C_2H_5OH solvent molecules varies from 8 to 1 as the ethanol

https://dx.doi.org/10.1021/acscatal.0c01328
ACS Catal. 2020, 10, 6771−6785

concentration is increased. For these calculations, the plane-wave energy cutoff was increased to 600 eV.

Frequency calculations were used to approximate zero-point vibrational energies (ZPVE), vibrational enthalpies (H_{vib}), and vibrational free energies (G_{vib}) of relevant gas-phase species and adsorbed guest species in the zeolite at 433 K. Two displacements per atom were used to calculate the Hessian with the finite difference method; all framework atoms except the Al site and its four surrounding O atoms were frozen in place. Low-frequency vibrations (<60 cm^{-1}) associated with frustrated translations and rotations were replaced with a value of 60 cm^{-1}, as low frequencies for guest species are inaccurate in zeolite frameworks but these motions still contribute to the enthalpies of guest species. The enthalpy and free energies of these species were calculated by summing the electronic energies from DFT (E_0) and the energies of dispersive interactions (E_d, from D3BJ[50]) with these vibrational (ZPVE, H_{vib}, G_{vib}) and frustrated translational (H_{tr}, G_{tr}) and rotational (H_{rot}, G_{rot}) energies

$$H = E_0 + E_d + \mathrm{ZPVE} + H_{vib} + H_{tr} + H_{rot} \quad (1)$$

$$G = E_0 + E_d + \mathrm{ZPVE} + G_{vib} + G_{tr} + G_{rot} \quad (2)$$

for all reactant, transition state, and product calculations. The translational and rotational enthalpies and free energies of gas-phase species were calculated from statistical mechanics, as shown by eqs S1−S10 in the Supporting Information.[62]

3. RESULTS AND DISCUSSION

3.1. Selectivities and Rates of EMF Formation on Brønsted Acid Catalysts. We evaluated HMF etherification with ethanol (C_2H_5OH) using several Brønsted acid catalysts. Consistent with previous reports, Amberlyst 15 (A15) achieved 76% selectivity to EMF at 84% HMF conversion (Table 1).[19,20] Because the reaction was carried out in the presence of 25 wt % water, the formation of acetals of HMF was suppressed, minimizing the potential for acetal-based routes to EMF formation.[63] EMF selectivity is nearly quantitative at low conversion and decreases with increasing conversion (Figure 1), predominantly due to the formation of ethyl levulinate (EL). For entries in Table 1 where the carbon balance does not close, the "missing" carbon is due to humin formation.[64] The formation of humins in particular is largely attributed to bimolecular self-condensation reactions that ultimately lead to tarry, polymeric materials,[65,66] although zeolite catalysts decrease the rate of humin formation for upgrading highly reactive furan derivatives.[67] HMF etherification is 95% selective to EMF at 66% HMF conversion on a beta zeolite (SiO_2:Al_2O_3 = 25, BEA-25), with nearly the same initial rate of EMF production as for A15 (Table 1). The other zeolite topologies evaluated here (FAU, MFI, and MOR), however, do not exhibit such high selectivities when they are measured at comparable conversion (Table 1), with FAU and MOR having selectivities near that of A15 (64%, 63%, and 76%, respectively), while MFI achieves 88% selectivity at 66% conversion. HMF etherification rates, furthermore, are higher for ethanol than for butanol, cyclohexanol, or phenol in BEA-25 catalysts under similar conditions (Figure 2). The differences in selectivity and EMF production rates for the catalysts studied here could result from acid site density effects, mass transport limitations in some catalysts, or catalyst topology and intrinsic kinetic behavior. We next evaluate each of these effects in turn.

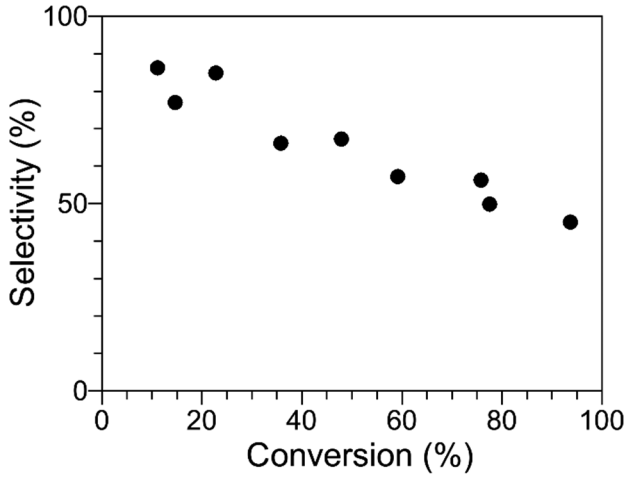

Figure 1. Influence of fractional conversion of HMF on selectivity to EMF in Amberlyst-15 (A15). The decrease in EMF selectivity with increasing HMF conversion suggests the presence of secondary reactions that consume EMF and high primary selectivities for the cross-etherification reaction. Reaction conditions: A15 catalyst, 4 mL of 200 mM HMF and 12.9 M C_2H_5OH in H_2O, HMF:cat. = 10:7 (g:g), 433 K.

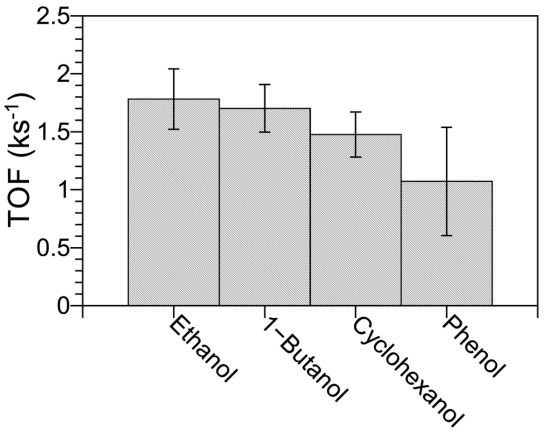

Figure 2. Influence of alcohol identity on the formation of HMF ethers. Reaction conditions: BEA-25 catalyst, 4 mL of 115 mM HMF and 12.9 M alcohol in H_2O, HMF:cat = 10:7 (g:g), 433 K, HMF conversion <15%.

The initial rates of EMF production were measured at HMF conversions below 15%. The specific rate of EMF production over A15 is nearly identical with that measured over BEA-25, consistent with the high selectivity observed at low conversion over both catalysts. Within the set of zeolites in Table 1, the rates and selectivities follow the same trend with respect to topology, with the rate of EMF production increasing in the order FAU < MFI < MOR < BEA. FTIR spectroscopy of adsorbed pyridine shows that the ratio of Brønsted to Lewis acid sites varies across this series of zeolites (Table S1). However, as shown in Figure S1, there is no clear trend in EMF selectivity with respect to the Lewis acid site density. Given the direct correlation of the EMF production rate with respect to Brønsted acid site density (*vide infra*), it is unsurprising that Lewis acidity does not strongly influence the EMF selectivity and suggests that, for the zeolites studied here, the rates of Lewis acid catalyzed reactions are small relative to the rates of Brønsted acid catalyzed reactions. The density of Brønsted acid sites also differs among these catalysts,

https://dx.doi.org/10.1021/acscatal.0c01328
ACS Catal. 2020, 10, 6771−6785

and some of the variation in the initial rate of EMF production can be attributed to differences in the number of sites available for reaction. The turnover frequency (TOF) accounts for differences in acid site density by normalizing the EMF formation rate by the number of Brønsted acid sites on each catalyst. The TOF for EMF production measured over A15 (0.94 ks^{-1}) is substantially higher than those measured over MFI, MOR, and FAU (~0.2 ks^{-1}); however, the TOF measured over BEA-25 is 1 order of magnitude greater than that measured over the other zeolites (2.7 ks^{-1}). The high TOF for EMF production over BEA-25, relative to the other materials, suggests that the enhanced selectivity observed for this catalyst is due in part to faster EMF production relative to the rate of byproduct formation. However, the constancy of the EMF production rate over MFI, MOR, and FAU—despite the significant differences in EMF selectivity across this series of catalysts—suggests that each catalyst exhibits a different rate of byproduct formation.

One potential explanation for the differences in the rates of byproduct formation is the presence of a concentration gradient within the BEA-25 crystallites, which would locally suppress the rate of bimolecular condensation. If such a gradient is present, then the TOF for EMF production should depend on the density of acid sites, which can be altered by varying the Al content of the zeolite. Accordingly, the rate of EMF production was measured using catalysts commercially available from Zeolyst, Inc., and compared to the Brønsted acid site densities reported in the literature for these catalysts as measured by temperature-programmed desorption of isopropylamine.[28,40] The selectivity to EMF is nearly constant for this series of materials (Table 1), and the rate of EMF formation is directly proportional to the number of acid sites (Figure 3).

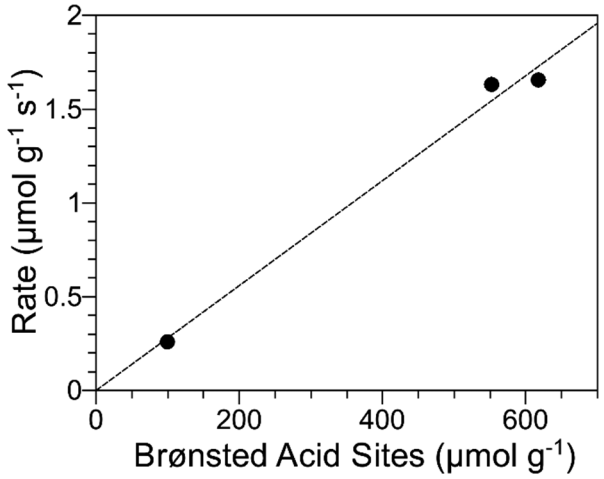

Figure 3. Influence of Brønsted acid site density on the rate of EMF production for three BEA samples. Reaction conditions: BEA-25, BEA-38, and BEA-300, 4 mL of 200 mM HMF and 12.9 M C_2H_5OH in H_2O, HMF:cat. = 10:7 (g:g), 433 K, HMF conversion <15%.

Therefore, there is no significant concentration gradient present in the BEA samples, and the high activity and the high selectivity to EMF observed over BEA cannot be caused by locally suppressed rates of bimolecular condensation. Apart from MFI, the other catalysts evaluated here all have pore diameters as large as or larger than that of BEA, suggesting they too lack concentration gradients during reactions. While the concentration of HMF in the pores of MFI may be nonuniform, the selectivity over this catalyst is comparable to that over FAU and MOR, likely due to reactions occurring on the external surface of the zeolite crystallite. Correspondingly, the BEA, FAU, and MOR catalysts meet the Koros−Nowack criterion for the absence of internal mass transfer effects, as described by Madon and Boudart,[71] indicating that the reaction kinetics data collected for the BEA samples are free of mass-transfer artifacts. Similarly, we have calculated the Weisz−Prater number, $N_{W\text{-}P}$, for EMF formation in BEA-25 (which has the highest specific reaction rate), as described by Vannice.[72] The value of $N_{W\text{-}P}$ for this catalyst is 0.002 for the conditions used in generating the data in Figure 3, which corresponds to an effectiveness factor of 99.97%, confirming the absence of concentration gradients within the zeolite crystallite. Notably, this value of $N_{W\text{-}P}$ is below the 0.3 criterion generally given for the absence of mass-transfer limitations.[72] Therefore, neither mass transfer limitations nor Brønsted acid site densities are responsible for differences in selectivity toward EMF over these catalysts. Figure S2 indicates that there is an optimum in EMF selectivity with respect to the constraint index,[73] which is an empirical parameter that is indicative of confinement effects due to the topology of zeolite catalysts. It is then likely that the high selectivity to EMF and the high rates observed over BEA zeolite are due to the unique topology of that catalyst. Notably, the kinetic diameter of HMF is ~6.2 Å[74] while the largest sphere that can be inscribed in the BEA framework is 6.9 Å in diameter,[75] suggesting that there may be a match between the geometry of the zeolite and the transition state for EMF formation.

3.2. Kinetics of EMF Formation on H-BEA. With mass transfer and site density effects having been eliminated, EMF selectivity can be governed by the intrinsic reaction kinetics for each catalyst. Here, we focus on elucidating the mechanism of cross-etherification of HMF and ethanol on H-BEA using both kinetics measurements and theory. Such a mechanistic analysis on a catalyst where few side products form must precede rigorous analyses of structural characteristics of these frameworks that dictate selectivity differences. Moreover, a full investigation on the kinetics of cross-etherification in each of these frameworks is beyond the scope of this study. The rate of EMF formation increases with HMF concentration (Figure 4a). Solvation effects can lead to nontrivial kinetics trends, which can be simplified by expressing the reaction rates in terms of activities.[76] Activities, α_i, can be expressed in a straightforward manner using activity coefficients estimated by the UNIFAC method,[77,78] and the rate data obtained here are plotted according to their UNIFAC activities in Figure 4b. The EMF formation rates are first order (0.98 ± 0.04) with respect to HMF activity, as shown by the dashed curve in Figure 4b. The HMF concentration and activity correlate to one another, as HMF is dilute (<1 mol %) across all conditions studied here, but changes in C_2H_5OH concentration will lead to nontrivial shifts in activity, as discussed later, prompting the use of activities in rate expressions. On the basis of the first-order behavior of HMF, it is unlikely that HMF monomers are abundant surface intermediates. Next, we consider the kinetic behavior of the various HMF etherification pathways.

Ether formation can proceed by three distinct pathways (Figure 5) that involve a total of four transition states. For each pathway, either ethanol or HMF can undergo dehydration (R_1OH and R_2OH can be HMF and C_2H_5OH, in either order). Each transition state can be kinetically relevant, and we describe these pathways and their rate expressions below.

https://dx.doi.org/10.1021/acscatal.0c01328
ACS Catal. 2020, 10, 6771−6785

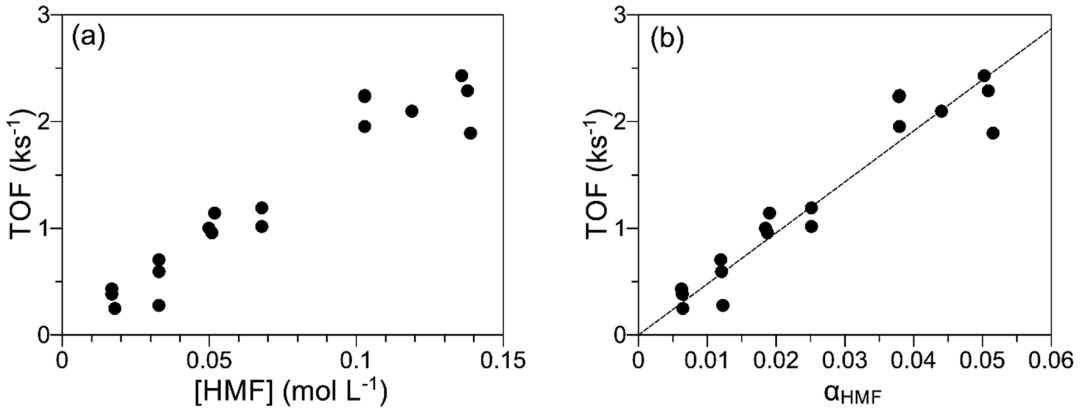

Figure 4. Dependence of the EMF production rate on HMF concentrations. The curve in (b) corresponds to a first-order fit to the rate data. Turnover frequencies (TOFs) are normalized to the number of protons in the BEA-25 catalyst (Table 1). Reaction conditions: BEA-25 catalyst, 4 mL of HMF and 12.9 M C_2H_5OH in H_2O, HMF:cat. = 10:7 (g:g), 433 K, HMF conversion <15%.

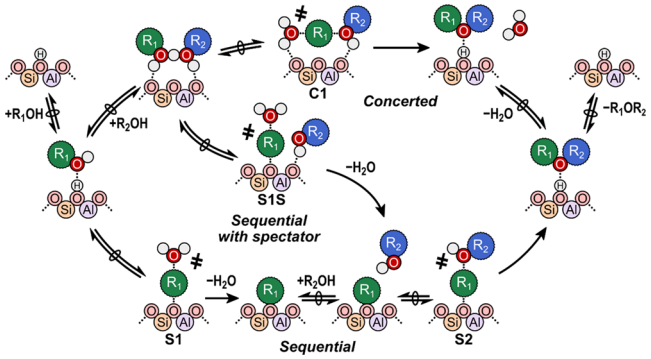

Figure 5. Ether formation mechanisms considered in this work. R_1 and R_2 represent either the methylfurfural or ethyl groups.

In the first potential pathway, the ether is formed according to a concerted S_N2 reaction mechanism (Figure 5, top). Given that there are two distinct alcohols, there are two routes by which this concerted mechanism can occur: via dehydration of either HMF or ethanol. The rate-controlling step is preceded by quasi-equilibrated adsorption of both alcohols and followed by the kinetically irrelevant desorption of water and EMF. If the surface is covered by adsorbed ethanol, by adsorbed HMF, and by ethanol−HMF pairs, then the corresponding rate equation for this concerted route is

$$\frac{r_{C1}}{[L]} = \frac{k_{C1}[R_1OH][R_2OH]}{1 + K_{R_1}[R_1OH] + K_{R_2}[R_2OH] + K_{D12}[R_1OH][R_2OH]} \quad (3)$$

where k_{C1} is the effective rate constant for forming the concerted transition state from a bare surface; K_{R1}, K_{R2}, and K_{D12} are the equilibrium constants for the adsorption of each alcohol and a protonated R_1OH-R_2OH pair, respectively; and $[L] = [*] + [R_1OH^*] + [R_2OH^*] + [R_1OH-R_2OH^*]$ is the site balance. The value of the rate constant, k_{C1}, is governed by whether EtOH or HMF undergoes dehydration, as those transition states have distinct carbenium ions and structures. However, the form of the S_N2 rate expression is identical for both cases. In a second pathway, one alcohol is dehydrated to form a surface alkyl species (Figure 5, bottom). This pathway is analogous to an S_N1 mechanism, where the surface alkyl is a reactive intermediate. If the rate-determining step of this mechanism is the alkylation of the zeolite surface, the corresponding rate equation is

$$\frac{r_{S1}}{[L]} = \frac{k_{S1}[R_1OH]}{1 + K_{R_1}[R_1OH] + K_{R_2}[R_2OH] + K_{D12}[R_1OH][R_2OH]} \quad (4)$$

where k_{S1} is the effective rate constant for surface alkylation. This rate equation is distinct from the kinetic expression for the concerted S_N2 pathway (eq 3). This surface alkylation reaction can also take place in the presence of a spectating alcohol species (Figure 5, middle), whose presence can affect the barrier (as shown previously for zeolite methylation near benzene and methanol).[79,80] The coadsorption of the second alcohol in this mechanism leads to a rate equation functionally identical to eq 3:

$$\frac{r_{S1S}}{[L]} = \frac{k_{S1S}[R_1OH][R_2OH]}{1 + K_{R_1}[R_1OH] + K_{R_2}[R_2OH] + K_{D12}[R_1OH][R_2OH]} \quad (5)$$

where k_{S1S} is the effective rate constant for surface alkylation with a spectating alcohol. Finally, these surface alkylation reactions are followed by a second step in which the EMF product is formed, and this step could be rate controlling if surface alkylation is quasi-equilibrated. Because water desorbs prior to ether formation in the sequential mechanisms, the second step is inhibited by water, as it reduces the coverage of surface alkyls; therefore, the rate equation takes the form

$$\frac{r_{S2}}{[L]} = \frac{k_{S2}[R_1OH][R_2OH][H_2O]^{-1}}{1 + K_{R_1}[R_1OH] + K_{R_2}[R_2OH] + K_{D12}[R_1OH][R_2OH]} \quad (6)$$

where k_{S2} is the effective rate constant for ether formation.

The functional forms of eqs 3 and 5 are identical, and for reactions in the aqueous phase they are identical with eq 6. Thus, if the reaction is limited by the transition states of the concerted pathway (step C1, eq 3), surface alkylation with a spectator (step S1S, eq 5), or ether formation from a surface alkyl species (step S2, eq 6), then the apparent reaction orders with respect to the alcohol concentrations would be the same.

https://dx.doi.org/10.1021/acscatal.0c01328
ACS Catal. 2020, 10, 6771−6785

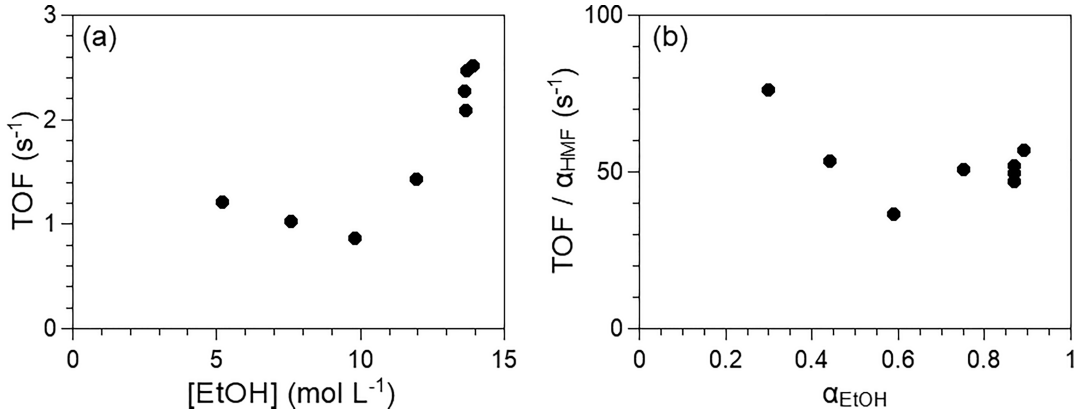

Figure 6. Dependence of the EMF production rate on ethanol concentration (a) and how the HMF-normalized rate depends on ethanol activity (b). TOFs are normalized to the number of protons on the BEA surface (see Table 1). Reaction conditions: BEA-25 catalyst, 4 mL of 200 mM HMF and varying concentrations of C_2H_5OH in H_2O, HMF:cat. = 10:7 (g:g), 433 K, HMF conversion <15%.

As such, kinetics studies can only assist in contrasting these scenarios with one in which surface alkylation occurs in the absence of coadsorbed alcohols and is rate-limiting (step S1, eq 4). If this step is rate-determining and involves the dehydration of ethanol (eq 4, $R_1OH = C_2H_5OH$), then the rate should not increase with HMF concentration, as observed, ruling out this pathway. Otherwise, all reaction pathways described above predict first-order behavior in HMF, consistent with the kinetics data (Figure 4b).

The ethanol concentration was also varied (from 5 to 14 M) to determine how ethanol influences HMF etherification rates. EMF formation rates are nearly constant at <10 M C_2H_5OH and increase with C_2H_5OH concentration >10 M (Figure 6a), an observation that is inconsistent with any rate equation derived above. However, these large changes in solvent composition with varying C_2H_5OH concentration also alter HMF activities (even though the HMF concentration remains constant) because of liquid-phase nonidealities. These shifts in HMF activities must be accounted for in EMF formation rates, and because EMF formation is first-order in HMF (Figure 4b) this can be accomplished conveniently by dividing those rates by the HMF activity (Figure 6b). By making this correction and plotting the rate data against C_2H_5OH activity, estimated with UNIFAC,[77,78] a clearer picture of the kinetic behavior emerges. Rates normalized by HMF activity decrease by ∼40% as the C_2H_5OH activity increases from 0.3 to 0.9, indicating that ethanol either has very little effect on the rates or weakly inhibits the reaction. The kinetic behavior of HMF and C_2H_5OH is consistent with concerted HMF dehydration as the sole rate-limiting step (eq 3, R_1OH = HMF) if H_2O-derived species are the most abundant surface intermediate (leading to first- and zero-order behavior in HMF and C_2H_5OH, respectively). The lack of ethanol adsorbed at acid sites is possible at low concentrations (∼8:1 H_2O:C_2H_5OH molar ratio) but less likely at high ethanol concentrations (∼1:1 H_2O:C_2H_5OH), as C_2H_5OH binding is expected to be stronger than H_2O binding. Importantly, the reaction kinetics data do not rule out other pathways (e.g., those described by eqs 3, 5, and 6); while those pathways involve ethanol, the influence of ethanol on rates will be approximately zero order if ethanol-derived species cover the acid sites. Accounting for the nonideality of the liquid phase allows for reasonable interpretations of the kinetics data; however, the exact mechanism cannot be derived through such interpretations alone.

3.3. DFT Calculations of HMF Etherification Pathways. We further investigate the mechanism of cross-etherification of HMF and ethanol using DFT calculations. These calculations, in conjunction with kinetics measurements, help determine the mechanism by which cross-etherification occurs in H-BEA as a preliminary explanation of its high selectivity toward EMF. We calculated free energies of the intermediates in each HMF etherification pathway (Figure 5) at a standard state (433 K, 1 bar of C_2H_5OH and HMF) in H-BEA. HMF binds more strongly to the acid sites than either ethanol or H_2O, with binding free energies of −54, −37, and −21 kJ mol^{-1}, respectively. Binding a second alcohol to these complexes is less favorable (e.g., the binding free energy of ethanol near HMF adsorbed to a proton (HMF*) is −23 kJ mol^{-1} in comparison to −37 kJ mol^{-1} in the absence of HMF*), as it results in sharing a proton between two weak bases. The base pairs, however, are strong enough to deprotonate the acid site, and we note that binding free energies remain negative for alcohol adsorption even in the presence of preadsorbed alcohols. These binding energies are calculated with gas-phase reference states (1 bar) despite the reactions occurring in the liquid phase. The errors inherent in this assumption are remedied in section 3.4; for now, intrinsic barriers will be examined for reactions described in Figure 5, as these intrinsic barriers are independent of the bulk properties (i.e., whether we use a gas or solvated bulk phase).

HMF dehydration occurs with a lower intrinsic barrier (96 kJ mol^{-1}) in comparison to ethanol dehydration (120 kJ mol^{-1}), likely because it occurs via a more stable carbocation (Figure 7). Dehydrating HMF to form a bound alkoxide occurs with an intrinsic barrier of 96 kJ mol^{-1} in the absence of ethanol and 116 kJ mol^{-1} in the presence of ethanol, indicating that coadsorbing ethanol makes surface alkylation by HMF dehydration more difficult, potentially because of repulsive steric interactions (Figure 7). Dehydrating ethanol to form ethoxide, in contrast, has an intrinsic barrier of 111 kJ mol^{-1} in the presence of HMF, which is 9 kJ mol^{-1} lower that than in its absence (120 kJ mol^{-1}), and the transition state structure (Figure S4d in the Supporting Information) shows that the leaving H_2O group H-bonds to HMF, which confers additional stabilization.

https://dx.doi.org/10.1021/acscatal.0c01328
ACS Catal. 2020, 10, 6771−6785

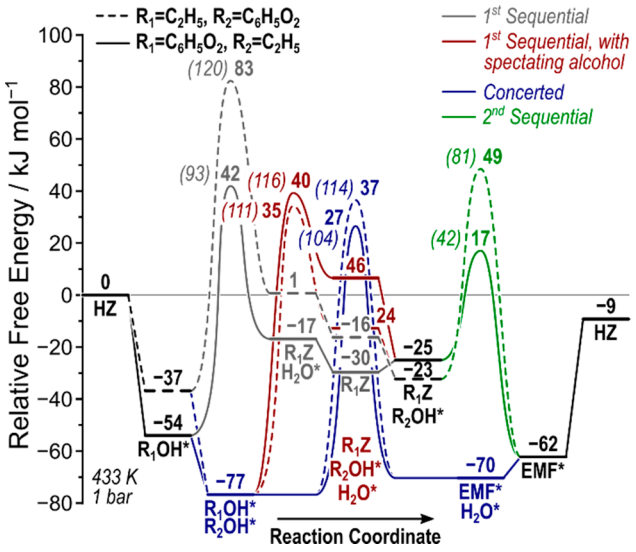

Figure 7. Free energies (433 K, 1 bar) for EMF formation through concerted and sequential pathways (Figure 5) relative to a bare proton and gas-phase species. Routes where R_1OH is C_2H_5OH (through C_2H_5OH dehydration) are dashed, and routes where R_1OH is HMF (through HMF dehydration) are solid. Intrinsic barriers (in kJ mol^{-1}) are shown in parentheses for each reaction.

The intrinsic barriers for concerted ether formation (104 and 114 kJ mol^{-1}) and for surface alkylation with a spectating alcohol (111 and 116 kJ mol^{-1}) are similar to one another and follow the same rate expression (eqs 3 and 5, respectively), rendering these pathways difficult to distinguish (Figure 7). Among them, concerted ether formation via HMF dehydration has the lowest barrier (104 kJ mol^{-1}).

The transition state structure for concerted EMF formation from HMF dehydration is similar to previously calculated transition states for concerted etherification of other alcohols.[35,36,79−84] The water and ethanol interact simultaneously with two different O atoms of the conjugate base (190 and 187 pm, respectively), while the methylfurfural cation (MF^+) is located between the water leaving group (216 pm) and the ethanol (236 pm; Figure 8). The methylfurfural carbocation forms a planar sp^2-hybridized C atom upon dehydration of HMF. The accessible resonance structures for this MF^+ species—shown in Figure S7 in the Supporting Information—reduce its ΔG_{act} value to form EMF (104 kJ mol^{-1}) in comparison to a ΔG_{act} value of 114 kJ mol^{-1} to form EMF via C_2H_5OH dehydration. While the concerted transition state via C_2H_5OH dehydration forms a structure similar to that via HMF dehydration with H bonds to the conjugate base (Figure S4b), the ethyl group cannot effectively redistribute its charge.

Generally, transition states which occur via a methylfurfural cation (MF^+)—i.e., from dehydrating HMF—are consistently lower in energy than those which occur via an ethyl cation for comparable routes (Figure 7), because the MF^+ cation has several resonance structures (Figure S7 in the Supporting Information) which favor its formation over that of an ethyl cation. This stability is confirmed by gas-phase calculations of alkyl transfers between two water molecules, which is barrierless for MF^+ but occurs with a barrier of 25 kJ mol^{-1} for ethyl transfer (Figure S8), demonstrating that MF^+ carbocations are more stable than ethyl carbenium ions.

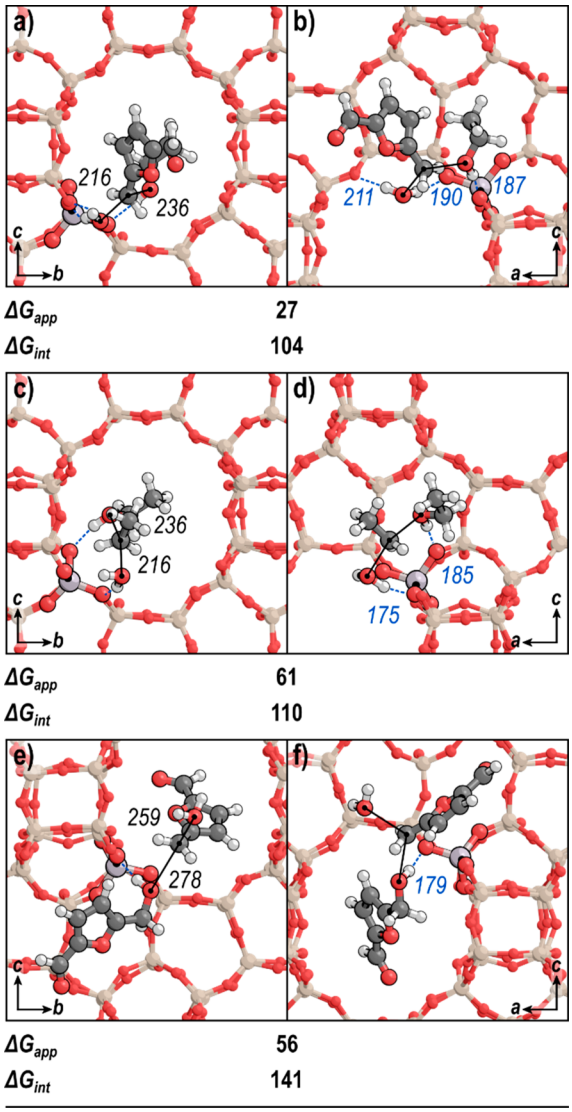

Figure 8. Structure of the transition state for concerted EMF formation via HMF dehydration shown (a) along the *a* vector of the BEA unit cell and (b) along the *b* vector of the BEA unit cell. Incipient and breaking bonds are indicated with black lines, and H bonds are indicated with dashed blue lines. Bond lengths are shown in pm. Intrinsic (ΔG_{int}) and apparent (ΔG_{app}, relative to a bare proton) free energy barriers are shown in kJ mol^{-1}. Additional structures are shown in Figures S3 and S4 in the Supporting Information.

Cross-etherification between HMF and C_2H_5OH to form EMF occurs with high selectivity at low conversion for both A15 and BEA-25 materials and at high conversions for the latter material, as it suppresses the secondary reactions which decrease selectivity with increasing conversion on A15 (Figure 1). Here, we contrast cross-etherification through a concerted S_N2 mechanism (via HMF dehydration) with the self-etherification of ethanol to form diethyl ether (DEE) and the self-etherification of HMF to form 5,5′-oxy(bismethylene)-2-furaldehyde (OBMF). Forming DEE from two coadsorbed ethanols occurs with an intrinsic barrier of 110 kJ mol^{-1}, or 6 kJ mol^{-1} higher than that to form EMF and 4 kJ mol^{-1} lower than dehydrating ethanol near HMF to form EMF (Figure 8b). Forming OBMF from two coadsorbed HMF molecules occurs with an intrinsic barrier of 141 kJ mol^{-1}, despite occurring through HMF dehydration to form a stable MF^+ carbocation

https://dx.doi.org/10.1021/acscatal.0c01328
ACS Catal. 2020, 10, 6771−6785

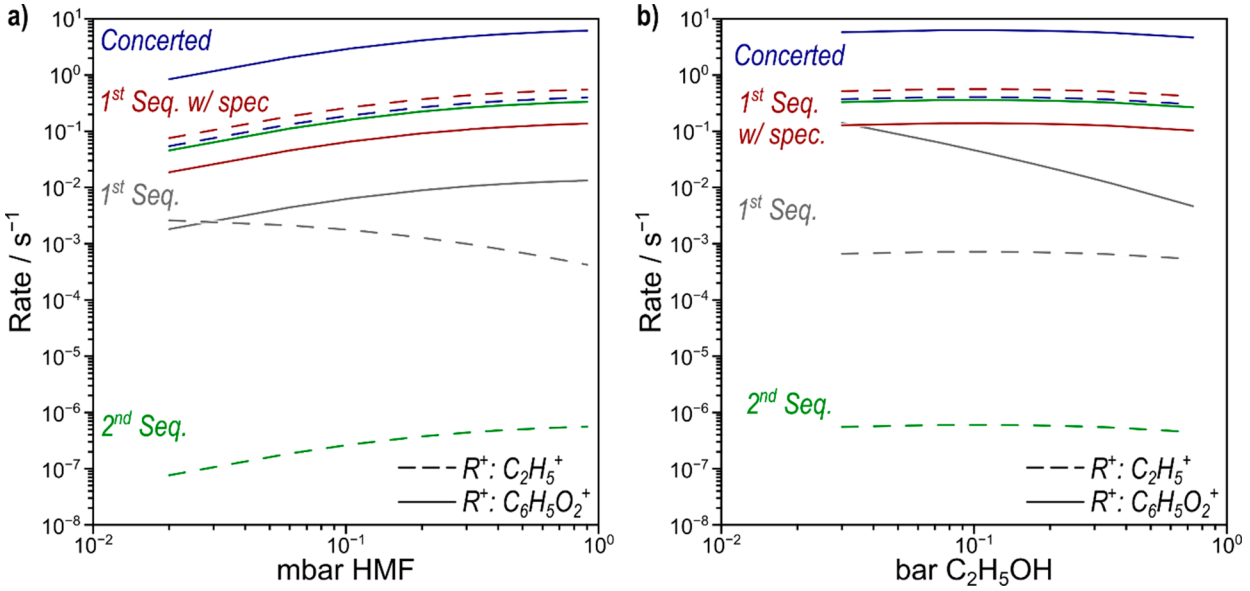

Figure 9. DFT-predicted rates as a function of (a) HMF pressure (at 0.34 bar of C_2H_5OH) and (b) C_2H_5OH pressure (at 0.54 mbar of HMF) at 433 K. Rates for the concerted reaction (blue), the first step of the sequential mechanism without a spectator (gray) and with a spectator (red), and the second step of the sequential mechanism (green) are shown for reactions via ethanol (dashed) or HMF (solid) dehydration.

(Figure 8c). The large barrier in spite of the stable carbocation suggests that this reaction is sterically or conformationally hindered in the BEA framework—i.e., it lacks the room to form the preferred S_N2 transition states observed for DEE and EMF formation. This crowding is also indicated by the low adsorption free energy of HMF near HMF (−8 kJ mol^{-1}), whereas adsorbing HMF near C_2H_5OH (−40 kJ mol^{-1}) or onto a bare proton (−54 kJ mol^{-1}) is much more favorable. Together, these lead to lower predicted rates of DEE and OBMF formation in comparison to that for EMF in BEA (Figure S9 in the Supporting Information). Generally, C_2H_5OH self-etherification is less favored than EMF formation because it must occur through an ethyl carbenium, which is less stable than the MF^+ carbenium, while HMF self-etherification is limited by the pores of the BEA zeolite.

The adsorption energies and thus the effective barriers for these pathways are calculated on the basis of an ideal gas phase composed of HMF and ethanol (433 K, 1 bar), whereas the kinetics data were collected in the aqueous phase. Here, we introduce a hypothetical vapor phase to reconcile this difference.

3.4. Unifying Experimental and Theoretical Results.

The presence of a highly nonideal liquid phase in kinetics measurements complicates comparisons between them and DFT calculations performed under vacuum. A common approach to reconcile these conditions is to simulate the liquid phase in the DFT calculations (e.g., by including solvent molecules and performing molecular dynamics calculations); however, this approach can prove to be computationally expensive. Static explicit or implicit solvation models, while computationally feasible, can give insights into how the solvent influences the potential energy and vibrational frequencies, but the ideal-gas formalisms for estimating translational and rotational entropies would be inappropriate for these liquid-phase reactions, rendering free energy estimations difficult. Instead, for each experimental condition we calculate the pressure of an equivalent, hypothetical ideal gas in equilibrium with the reacting liquid phase and use this value to determine the chemical potential. Chemical potentials, μ_i, are directly related to fugacities, f_i, by

$$\mu_i = \mu_i^\circ + RT \ln \hat{f}_i \tag{7}$$

where μ_i^o corresponds to the chemical potential of a pure species at unit fugacity, R is the ideal gas constant, and T is the reaction temperature.[85] We have adopted the notation of Smith and Van Ness,[77] wherein the circumflex operator (^) is used to represent values of species in mixtures. Any influence of the mixture on the chemical potential of species i is captured in the fugacity term, which can be calculated by any convenient means. The fugacity for the liquid phase can be assumed to be in equilibrium with a hypothetical vapor phase, such that $\hat{f}_i^l = \hat{f}_i^v$, which also requires that the temperature and pressure of the hypothetical vapor phase match those in the real liquid phase. For these conditions (1 atm and 433 K), it is reasonable to assume that the vapor phase is an ideal gas, for which the fugacity is simply the partial pressure, p_i, determined by the modified Raoult's law formulation of vapor−liquid equilibrium:[77]

$$y_i \hat{\phi}_i P = x_i \gamma_i f_i \tag{8}$$

where x_i and y_i correspond to liquid and vapor mole fractions, respectively, P corresponds to the total system pressure, $\hat{\phi}_i$ to the fugacity coefficient of species i, and f_i corresponds to the fugacity of pure i. For a liquid, f_i can be rewritten in terms of the saturation pressure, P_i^{sat}, and the fugacity coefficient at saturation, ϕ_i^{sat}. As y_iP is the partial pressure, p_i, of a compound, combining the fugacity coefficients into a ratio, $\Phi_i = \hat{\phi}_i/\phi_i^{sat}$, and recognizing the Poynting factor should be negligible at 1 bar leads to

$$p_i = \frac{x_i \gamma_i P_i^{sat}}{\Phi_i} \tag{9}$$

For ideal gases $\Phi_i = 1$, so that the equivalent pressures can be calculated solely from the experimental mole fractions (x_i), the activity coefficients (γ_i) predicted by UNIFAC,[78] and the

https://dx.doi.org/10.1021/acscatal.0c01328
ACS Catal. 2020, 10, 6771−6785

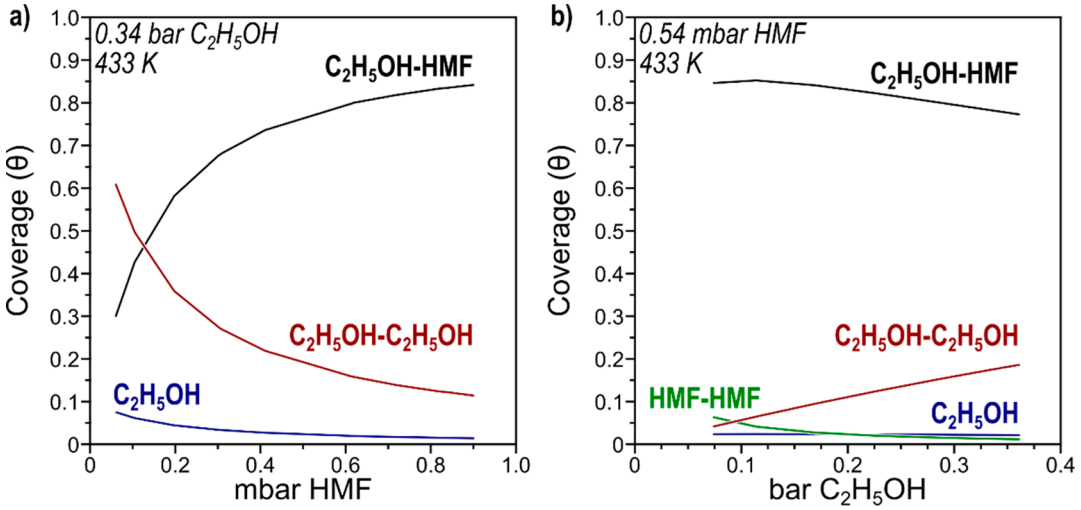

Figure 10. DFT-predicted surface coverages as a function of (a) HMF pressure (at 0.34 bar of C_2H_5OH) and (b) C_2H_5OH pressure (at 0.54 mbar HMF) at 433 K. The species considered were as follows: bare protons, adsorbed HMF, C_2H_5OH, and H_2O; dimeric complexes of HMF, C_2H_5OH, and H_2O; mixed complexes (C_2H_5OH–HMF, C_2H_5OH–H_2O, and HMF–H_2O). Species covering less than 1% of the surface are not shown for clarity.

saturation vapor pressures (P_i^{sat}) at the reaction temperature given by tabulated Antoine coefficients.[86] These virtual partial pressures enable DFT analysis using gas-phase statistical mechanics equations and bulk (vacuum) calculations. Because the hypothetical gas phase and liquid phase are considered to be in equilibrium with one another, their chemical potentials are equivalent. Therefore, free energies for this hypothetical gas phase calculated from DFT and statistical mechanics should match experimental observations when the reaction rates are written as a function of calculated chemical activity (which is proportional to the partial pressure of species i in the hypothetical ideal gas calculated in eq 9). Activity coefficients (UNIFAC) and partial pressures (eq 9) are shown in Table S2 in the Supporting Information for all experimental conditions used in this work.

We analyze DFT-calculated adsorption, reaction, and activation free energies using the maximum rate analysis approach. A maximum rate analysis evaluates each step in a reaction mechanism as if it were rate-controlling, with all preceding steps assumed to be quasi-equilibrated.[87] Here, rates at a variety of imposed pressures can be calculated from relevant rate equations (eqs 3–6), which were derived by assuming each of the four transition states shown in Figure 4 are kinetically relevant.

DFT-predicted maximum rates at partial pressures derived from the thermodynamic relationships described above are shown in Figure 9. These maximum rates can be used to determine which steps are quasi-equilibrated and which are kinetically relevant for the two-step sequential mechanisms. Rates for each step are calculated as through that step were rate-limiting in its appropriate pathway; among these rates, the slowest is the rate-determining step. This consideration, however, is not very relevant in this case, as these results show that the concerted S_N2 reaction via HMF dehydration occurs with rates >10× greater than the maximum rate of any other elementary step. The next fastest pathway is the concerted S_N2 reaction via C_2H_5OH dehydration, which occurs at rates ∼15× lower than the concerted pathway (n.b., while the first step of the sequential mechanism is faster than concerted C_2H_5OH dehydration, reactive flux through that pathway is limited by the slow rate of the second step). These two reactions both start with a C_2H_5OH–HMF complex coadsorbed to an acid site, and thus their relative rates are a function only of their intrinsic activation free energies (104 and 114 kJ mol^{-1}) and are independent of reaction conditions. On the basis of UNIFAC-derived partial pressures for these species under the conditions of these experiments (Table S2), this further indicates that the concerted route via this MF^+ transition state prevails under all conditions tested experimentally.

DFT-predicted adsorption free energies for HMF, C_2H_5OH, and H_2O along with their coadsorption free energies to form three homodimer (HMF–HMF, C_2H_5OH–C_2H_5OH, and H_2O–H_2O) and three mixed-dimer complexes (HMF–C_2H_5OH, C_2H_5OH–H_2O, HMF–H_2O, Figures S5 and S6 in the Supporting Information) can be used to predict the most abundant surface intermediates as a function of HMF and C_2H_5OH pressure. C_2H_5OH dimers make up over half the surface intermediates at 0.34 bar of C_2H_5OH and <0.15 mbar of HMF (Figure 10a), which is a 2000:1 pressure ratio (C_2H_5OH:HMF), corresponding to a concentration ratio of 560:1 in the nonideal solution. At higher HMF activities, the C_2H_5OH–HMF mixed complex covers half the surface, with coverages approaching 1 ML as HMF activity increases over the range of this study (corresponding to the high HMF concentration data points in Figure 4). No other species (of the 10 considered) make up more than 10% of the surface within the domain of experimental conditions tested in this work, and bare protons are essentially absent, as expected.

These surface coverages are used in the maximum rate analyses, and thus the reaction orders in HMF and ethanol are predicted by these techniques. Predicted EMF formation rates (Figure 9) increase with increasing HMF activity, and the reaction order shifts from first (at low HMF pressures) toward zero (at high HMF) in a typical Langmuir–Hinshelwood–Hougen–Watson fashion as the surface shifts from being covered by C_2H_5OH–C_2H_5OH complexes to C_2H_5OH–HMF complexes (Figure 10). The rates are nearly independent of ethanol pressure at constant HMF activity with slight inhibition at higher ethanol pressures, consistent with a shift

https://dx.doi.org/10.1021/acscatal.0c01328
ACS Catal. 2020, 10, 6771–6785

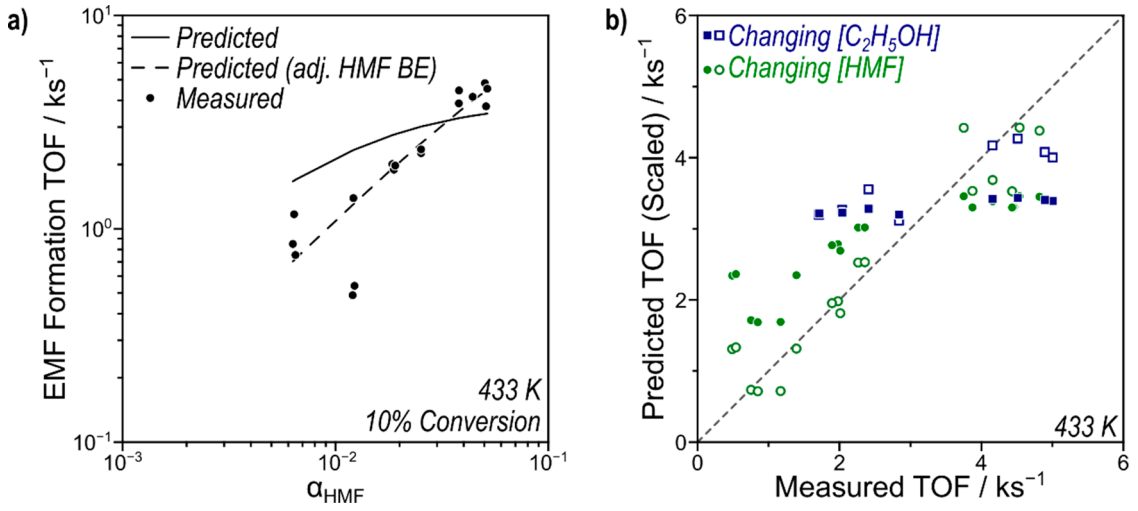

Figure 11. (a) Measured (dots) and predicted (solid line, scaled by 5.2×10^{-4}) EMF formation rates in BEA (433 K, <10% HMF conversion) as a function of HMF activity. Predicted rates after adjustment of HMF binding energy by 10 kJ mol^{-1} are represented by a dashed line and scaled by 1.0×10^{-3}. (b) Parity plot of EMF formation rates while HMF concentration (green circles) and C_2H_5OH concentration (blue squares) were varied . Hollow symbols are those after adjusting HMF binding energies by 10 kJ mol^{-1}; filled symbols are unadjusted. Predicted rates are multiplied by 5.2×10^{-4} (unadjusted) and 1.0×10^{-3} (adjusted).

in the surface from C_2H_5OH–HMF to C_2H_5OH–C_2H_5OH as the C_2H_5OH pressure increases. Because the transition state involves C_2H_5OH and HMF under all reaction conditions, the reaction order depends only on whether the surface is covered by C_2H_5OH–C_2H_5OH, in which case the rates are promoted by HMF and inhibited by C_2H_5OH, or the surface is covered by C_2H_5OH–HMF, in which case the rates are zero order in both species.

These DFT-predicted rates can be compared to experimentally measured rates to assess whether they capture the correct trends. The experimental rates are approximately first order in HMF activity, while the DFT-predicted rates are sublinear in HMF activity (Figure 11a). This trend suggests that the HMF binding energy is overpredicted by DFT methods (the free energy of adsorption is too exergonic), leading to high C_2H_5OH–HMF coverages (and thus zero-order kinetics) at lower than measured HMF:C_2H_5OH ratios. If the adsorption free energy of HMF is increased *ad hoc* from −54 to −44 kJ mol^{-1}, then the predicted C_2H_5OH-HMF coverage decreases (C_2H_5OH–C_2H_5OH increases) and rates become first order in HMF over the entire activity range. Such overprediction of the binding energy was also observed for benzene alkylation reactions (where the benzene binding energy was too exergonic).[79] This overestimation is likely caused by an overestimation of the dispersive interactions by the D3 correction, which affects larger molecules (e.g., HMF) more than smaller species (e.g., C_2H_5OH). Unlike variations in HMF concentration, variations in C_2H_5OH concentration change the UNIFAC-derived activities (and therefore partial pressures) of HMF (Table S2); therefore, we directly compare DFT-predicted rates while accounting for these thermodynamic nonidealities (Figure 11b). DFT-predicted rates are approximately invariant as the concentration of C_2H_5OH changes (causing both the C_2H_5OH and HMF partial pressures to vary), while measured rates increase by a factor of ∼3. This leads to a large deviation from parity and qualitative disagreement between DFT-predicted rates and measured rates, particularly at low ethanol concentrations. Notably, the adjustment of the HMF binding energy also improves the qualitative agreement of the data gathered at varying C_2H_5OH concentrations. These DFT data are scaled by ∼3 orders of magnitude to facilitate these qualitative comparisons. The large deviations between the quantitative and measured data are likely caused by an overestimation of the binding energies of all complexes in this solvent-free BEA framework with the D3 dispersion corrections mentioned earlier. Implicit solvent modeling with VASPsol increases the predicted rates, indicating that these errors are not associated with the lack of implicit solvent within the pores (Figure S10 in the Supporting Information).

This mechanistic investigation indicates a preference for concerted etherification routes via a MF$^+$ cation in BEA. Such a transition state might be unfavorable in the other frameworks tested here, which have smaller pores that could be too small for this transition state to form (MFI and the 8-MR of MOR; Table 2) or larger pores which might not effectively solvate the transition state (FAU and the 12-MR of MOR; Table 2). This specificity is typical of zeolite catalysts, whose voids stabilize transition states more effectively as the void approaches the size of the relevant transition state.[88−96] Experimental evidence for such matching between the size of the transition state and the void size is found in Figure S2, which shows that the highest selectivity for EMF is obtained for the zeolite (BEA) with an intermediate constraint index, and lower EMF selectivities are obtained for low (FAU and MOR) and high

Table 2. Zeolite Frameworks Tested in This Work and Their Pore Dimensions from the Atlas of Zeolite Frameworks[97]

framework	ring	dimensions (Å)
BEA	12-MR along [100] and [010]	6.6 × 6.7
	12-MR along [001]	5.6 × 5.6
FAU	12-MR	7.4 × 7.4
MFI	straight 10-MR	5.5 × 5.1
	sinusoidal 10-MR	5.6 × 5.3
MOR	12-MR	7.0 × 6.5
	8-MR	5.7 × 2.6

https://dx.doi.org/10.1021/acscatal.0c01328
ACS Catal. 2020, 10, 6771−6785

(MFI) constraint index zeolites. Therefore, these results indicate that the high selectivity in BEA arises because its pores most effectively solvate the preferred transition state—concerted HMF dehydration—for cross-etherification.

4. CONCLUSIONS

We have observed that H-BEA zeolite achieves nearly quantitative selectivity for the formation of ethoxymethylfurfural (EMF, a biodiesel additive) from 5-hydroxymethylfurfural (HMF) and ethanol in an aqueous solvent system. We attribute this high selectivity to the unique reactivity of HMF over BEA, which exhibits a higher TOF for etherification (2.6–2.9 ks^{-1}) in comparison to other H-form zeolites (MFI, FAU, and MOR; TOFs ranging from 0.19 to 0.21 ks^{-1}). BEA is also more active, on a TOF basis, than Amberlyst 15 (0.94 ks^{-1}), which achieves only ∼75% selectivity to EMF. This rate enhancement on BEA does not occur as a result of mass transport limitations on BEA. The overall rate of EMF formation increases with Brønsted acid site density in BEA, indicating the absence of a concentration gradient of the reactants within the BEA crystals.

The rate of EMF formation in BEA is first order with respect to HMF concentration, but we observed the rate to vary in a nontrivial fashion over a large range of ethanol concentrations. We showed that this variation is due to thermodynamic nonidealities induced by the mixed alcohol/water solvent used for the reaction, and the rates are inhibited by increasing thermodynamic activity of ethanol, consistent with stable ethanol-related species blocking sites on the BEA surface. These nonidealities also hinder the direct comparison of theoretical and experimental results to explain the observed kinetics. However, calculation of equivalent partial pressures in a hypothetical ideal gas phase in equilibrium with the liquid phase allows for direct calculation of rates from density functional theory (DFT), which can in turn be compared with the experimental rates measured in the aqueous phase.

Using this approach, we have shown that a concerted etherification mechanism proceeding through HMF dehydration prevails under all experimental conditions. This concerted route has an overall free energy barrier of 27 kJ mol^{-1} relative to a bare proton from DFT-calculated energies (433 K, 1 bar). DFT-predicted rates show sublinear behavior with respect to HMF activity and zero-order behavior with respect to ethanol activity, only partially consistent with experimental rates. This discrepancy is likely due to overprediction of the binding strength of HMF; by an artificial increase in the binding free energy of HMF from −54 to −44 kJ mol^{-1}, good qualitative agreement between DFT-predicted rates and observed kinetics is obtained. Critically, we show that the reactivity of HMF in zeolite catalysts in an aqueous medium is dominated by carbenium ion chemistry, rather than the Lewis acidity that the literature suggests may prevail under anhydrous conditions.

■ ASSOCIATED CONTENT

Supporting Information

The Supporting Information is available free of charge at https://pubs.acs.org/doi/10.1021/acscatal.0c01328.

Measurement of Lewis acid sites by FTIR spectroscopy of adsorbed pyridine, estimations of free energies, enthalpies, and entropies from DFT, tabulation of activity coefficients, activities, and equivalent pressures, DFT-calculated structures of transition states and surface intermediates, gas-phase carbocation exchange energetics,and DFT-predicted rates with adjusted permittivities from VASPsol (PDF)

■ AUTHOR INFORMATION

Corresponding Authors

David Hibbitts − *Department of Chemical Engineering, University of Florida, Gainesville, Florida 32612, United States;* orcid.org/0000-0001-8606-7000; Email: hibbitts@che.ufl.edu

Thomas J. Schwartz − *Department of Chemical and Biomedical Engineering, Forest Bioproducts Research Institute, and Frontier Institute for Research in Sensor Technology, University of Maine, Orono, Maine 04469, United States;* orcid.org/0000-0002-2788-8519; Email: thomas.schwartz@maine.edu

Authors

Meredith C. Allen − *Department of Chemical and Biomedical Engineering and Forest Bioproducts Research Institute, University of Maine, Orono, Maine 04469, United States*

Alexander J. Hoffman − *Department of Chemical Engineering, University of Florida, Gainesville, Florida 32612, United States;* orcid.org/0000-0002-1337-9297

Tsung-wei Liu − *Department of Chemical Engineering, University of Florida, Gainesville, Florida 32612, United States*

Matthew S. Webber − *Department of Chemical and Biomedical Engineering, University of Maine, Orono, Maine 04469, United States*

Complete contact information is available at: https://pubs.acs.org/10.1021/acscatal.0c01328

Author Contributions

The manuscript was written through contributions of all authors. All authors have given approval to the final version of the manuscript.

Author Contributions

⊥M.C.A. and A.J.H. contributed equally.

Funding

USDA NIFA Grant No. 2018-67010-27905, ACS PRF DNI Grant No. 57079DNI5, NSF Grant No. ACI-1548562 through allocation CTS160041.

Notes

The authors declare no competing financial interest.

■ ACKNOWLEDGMENTS

The authors thank Akbar Mahdavi-Shakib, Spencer Martell, and Brian G. Frederick for assistance in collecting the FTIR spectra of adsorbed pyridine and Nick Hill, Christa Meulenberg, Aiden Crane, and Logan Doucette for assistance with the reaction kinetics measurements. Work at the University of Maine was supported in part by the University of Maine Office of the Vice President for Research and in part by an AFRI Lignin and Nanocellulose Products Challenge Area Grant No. 2018-67010-27905 from the USDA National Institute of Food and Agriculture. Any opinions, findings, conclusions, or recommendations expressed in this publication are those of the author(s) and do not necessarily reflect the view of the U.S. Department of Agriculture. Work at the University of Florida was partially funded by the ACS Petroleum Research Fund New Doctoral Investigation Award (57079DNI5). This work also used the Extreme Science and Engineering Discovery Environment (XSEDE), which is

supported by the National Science Foundation grant number ACI-1548562 through allocation CTS160041. Additional computational resources were provided by the University of Florida Research Computing.

REFERENCES

(1) Isikgor, F. H.; Becer, C. R. Lignocellulosic biomass: a sustainable platform for the production of bio-based chemicals and polymers. *Polym. Chem.* **2015**, *6* (25), 4497−4559.
(2) Shanks, B. H.; Keeling, P. L. Bioprivileged molecules: creating value from biomass. *Green Chem.* **2017**, *19*, 3177.
(3) Huber, G. W.; Iborra, S.; Corma, A. Synthesis of Transportation Fuels from Biomass: Chemistry, Catalysts, and Engineering. *Chem. Rev.* **2006**, *106* (9), 4044−4098.
(4) Schwartz, T. J.; Shanks, B. H.; Dumesic, J. A. Coupling chemical and biological catalysis: a flexible paradigm for producing biobased chemicals. *Curr. Opin. Biotechnol.* **2016**, *38*, 54−62.
(5) Siirola, J. J. The impact of shale gas in the chemical industry. *AIChE J.* **2014**, *60* (3), 810−819.
(6) Luterbacher, J. S.; Martin Alonso, D.; Dumesic, J. A. Targeted chemical upgrading of lignocellulosic biomass to platform molecules. *Green Chem.* **2014**, *16* (12), 4816−4838.
(7) Werpy, T.; Peterson, G. *Top value added chemicals from biomass: Volume I--Results of Screening for Potential Candidates from Sugars and Synthesis Gas*; 2004, DOE/GO-102004-1992.
(8) Saha, B.; Abu-Omar, M. M. Advances in 5-hydroxymethylfurfural production from biomass in biphasic solvents. *Green Chem.* **2014**, *16* (1), 24−38.
(9) Tong, X.; Li, Y. Efficient and Selective Dehydration of Fructose to 5-Hydroxymethylfurfural Catalyzed by Brønsted-Acidic Ionic Liquids. *ChemSusChem* **2010**, *3* (3), 350−355.
(10) Carniti, P.; Gervasini, A.; Biella, S.; Auroux, A. Niobic acid and niobium phosphate as highly acidic viable catalysts in aqueous medium: Fructose dehydration reaction. *Catal. Today* **2006**, *118* (3), 373−378.
(11) Roman-Leshkov, Y.; Chheda, J. N.; Dumesic, J. A. Phase Modifiers Promote Efficient Production of Hydroxymethylfurfural from Fructose. *Science* **2006**, *312* (5782), 1933−1937.
(12) Weingarten, R.; Rodriguez - Beuerman, A.; Cao, F.; Luterbacher, J. S.; Alonso, D. M.; Dumesic, J. A.; Huber, G. W. Selective Conversion of Cellulose to Hydroxymethylfurfural in Polar Aprotic Solvents. *ChemCatChem* **2014**, *6* (8), 2229−2234.
(13) Gallo, J. M. R.; Alamillo, R.; Dumesic, J. A. Acid-functionalized mesoporous carbons for the continuous production of 5-hydroxymethylfurfural. *J. Mol. Catal. A: Chem.* **2016**, *422*, 13−17.
(14) Gallo, J. M. R.; Alonso, D. M.; Mellmer, M. A.; Dumesic, J. A. Production and upgrading of 5-hydroxymethylfurfural using heterogeneous catalysts and biomass-derived solvents. *Green Chem.* **2013**, *15* (1), 85−90.
(15) Nikolla, E.; Román-Leshkov, Y.; Moliner, M.; Davis, M. E. One-Pot" Synthesis of 5-(Hydroxymethyl)furfural from Carbohydrates using Tin-Beta Zeolite. *ACS Catal.* **2011**, *1* (4), 408−410.
(16) Motagamwala, A. H.; Huang, K.; Maravelias, C. T.; Dumesic, J. A. Solvent system for effective near-term production of hydroxymethylfurfural (HMF) with potential for long-term process improvement. *Energy Environ. Sci.* **2019**, *12* (7), 2212−2222.
(17) van Putten, R.-J.; van der Waal, J. C.; de Jong, E.; Rasrendra, C. B.; Heeres, H. J.; de Vries, J. G. Hydroxymethylfurfural, A Versatile Platform Chemical Made from Renewable Resources. *Chem. Rev.* **2013**, *113* (3), 1499−1597.
(18) Shylesh, S.; Gokhale, A. A.; Ho, C. R.; Bell, A. T. Novel Strategies for the Production of Fuels, Lubricants, and Chemicals from Biomass. *Acc. Chem. Res.* **2017**, *50* (10), 2589−2597.
(19) Balakrishnan, M.; Sacia, E. R.; Bell, A. T. Etherification and reductive etherification of 5-(hydroxymethyl)furfural: 5-(alkoxymethyl)furfurals and 2,5-bis(alkoxymethyl)furans as potential bio-diesel candidates. *Green Chem.* **2012**, *14* (6), 1626−1634.
(20) Sacia, E. R.; Balakrishnan, M.; Bell, A. T. Biomass conversion to diesel via the etherification of furanyl alcohols catalyzed by Amberlyst-15. *J. Catal.* **2014**, *313*, 70−79.
(21) Mascal, M.; Nikitin, E. B. Direct, High-Yield Conversion of Cellulose into Biofuel. *Angew. Chem., Int. Ed.* **2008**, *47* (41), 7924−7926.
(22) Lanzafame, P.; Temi, D. M.; Perathoner, S.; Centi, G.; Macario, A.; Aloise, A.; Giordano, G. Etherification of 5-hydroxymethyl-2-furfural (HMF) with ethanol to biodiesel components using mesoporous solid acidic catalysts. *Catal. Today* **2011**, *175* (1), 435−441.
(23) Lew, C. M.; Rajabbeigi, N.; Tsapatsis, M. One-Pot Synthesis of 5-(Ethoxymethyl)furfural from Glucose Using Sn-BEA and Amberlyst Catalysts. *Ind. Eng. Chem. Res.* **2012**, *51* (14), 5364−5366.
(24) Lanzafame, P.; Barbera, K.; Papanikolaou, G.; Perathoner, S.; Centi, G.; Migliori, M.; Catizzone, E.; Giordano, G. Comparison of H + and NH4+ forms of zeolites as acid catalysts for HMF etherification. *Catal. Today* **2018**, *304*, 97−102.
(25) Salminen, E.; Kumar, N.; Virtanen, P.; Tenho, M.; Paivi, M.-A.; Mikkola, J.-P. Etherification of 5-Hydroxymethylfurfural to a Biodiesel Component Over Ionic Liquid Modified Zeolites. *Top. Catal.* **2013**, *56* (9−10), 765−769.
(26) Arias, K. S.; Climent, M. J.; Corma, A.; Iborra, S. Biomass-Derived Chemicals: Synthesis of Biodegradable Surfactant Ether Molecules from Hydroxymethylfurfural. *ChemSusChem* **2014**, *7* (1), 210−220.
(27) Lewis, J. D.; Van de Vyver, S.; Crisci, A. J.; Gunther, W. R.; Michaelis, V. K.; Griffin, R. G.; Román-Leshkov, Y. A Continuous Flow Strategy for the Coupled Transfer Hydrogenation and Etherification of 5-(Hydroxymethyl)furfural using Lewis Acid Zeolites. *ChemSusChem* **2014**, *7* (8), 2255−2265.
(28) Luo, J.; Yu, J.; Gorte, R. J.; Mahmoud, E.; Vlachos, D. G.; Smith, M. A. The effect of oxide acidity on HMF etherification. *Catal. Sci. Technol.* **2014**, *4* (9), 3074−3081.
(29) Lanzafame, P.; Papanikolaou, G.; Barbera, K.; Centi, G.; Perathoner, S. Etherification of HMF to biodiesel additives: The role of NH4+ confinement in Beta zeolites. *J. Energy Chem.* **2019**, *36*, 114.
(30) Gould, N. S.; Xu, B. Effect of liquid water on acid sites of NaY: An in situ liquid phase spectroscopic study. *J. Catal.* **2016**, *342*, 193−202.
(31) Gould, N. S.; Xu, B. Quantification of acid site densities on zeolites in the presence of solvents via determination of extinction coefficients of adsorbed pyridine. *J. Catal.* **2018**, *358*, 80−88.
(32) Smith, M. B.; March, J. *March's Advanced Organic Chemistry*, 6th ed.; Wiley-Interscience: Hoboken, NJ, 2007.
(33) Rorrer, J.; He, Y.; Toste, F. D.; Bell, A. T. Mechanism and kinetics of 1-dodecanol etherification over tungstated zirconia. *J. Catal.* **2017**, *354*, 13−23.
(34) Rorrer, J.; Pindi, S.; Toste, F. D.; Bell, A. T. Effect of Alcohol Structure on the Kinetics of Etherification and Dehydration over Tungstated Zirconia. *ChemSusChem* **2018**, *11* (18), 3104−3111.
(35) Carr, R. T.; Neurock, M.; Iglesia, E. Catalytic consequences of acid strength in the conversion of methanol to dimethyl ether. *J. Catal.* **2011**, *278* (1), 78−93.
(36) Knaeble, W.; Iglesia, E. Kinetic and Theoretical Insights into the Mechanism of Alkanol Dehydration on Solid Brønsted Acid Catalysts. *J. Phys. Chem. C* **2016**, *120* (6), 3371−3389.
(37) DeWilde, J. F.; Chiang, H.; Hickman, D. A.; Ho, C. R.; Bhan, A. Kinetics and Mechanism of Ethanol Dehydration on γ-Al2O3: The Critical Role of Dimer Inhibition. *ACS Catal.* **2013**, *3* (4), 798−807.
(38) Kijenski, J.; Baiker, A. Acidic sites on catalyst surfaces and their determination. *Catal. Today* **1989**, *5*, 1−119.
(39) Emeis, C. A. Determination of integrated molar extinction coefficients for infrared absorption bands of pyridine adsorbed on solid acid catalysts. *J. Catal.* **1993**, *141*, 347−54.
(40) Abdelrahman, O. A.; Vinter, K. P.; Ren, L.; Xu, D.; Gorte, R. J.; Tsapatsis, M.; Dauenhauer, P. J. Simple quantification of zeolite acid site density by reactive gas chromatography. *Catal. Sci. Technol.* **2017**, *7* (17), 3831−3841.

https://dx.doi.org/10.1021/acscatal.0c01328
ACS Catal. 2020, 10, 6771−6785

(41) Farneth, W. E.; Gorte, R. J. Methods for Characterizing Zeolite Activity. *Chem. Rev.* **1995**, *95*, 615−635.
(42) Kresse, G.; Furthmüller, J. Efficiency of ab-initio total energy calculations for metals and semiconductors using a plane-wave basis set. *Comput. Mater. Sci.* **1996**, *6* (1), 15−50.
(43) Kresse, G.; Furthmüller, J. Efficient iterative schemes for ab initio total-energy calculations using a plane-wave basis set. *Phys. Rev. B: Condens. Matter Mater. Phys.* **1996**, *54* (16), 11169−11186.
(44) Kresse, G.; Hafner, J. Ab initio molecular-dynamics simulation of the liquid-metal–amorphous-semiconductor transition in germanium. *Phys. Rev. B: Condens. Matter Mater. Phys.* **1994**, *49* (20), 14251−14269.
(45) Kresse, G.; Hafner, J. Ab initio molecular dynamics for liquid metals. *Phys. Rev. B: Condens. Matter Mater. Phys.* **1993**, *47* (1), 558−561.
(46) Kravchenko, P.; Plaisance, C.; Hibbitts, D., A New Computational Interface for Catalysis. *ChemRxiv* **2019**.
(47) Blöchl, P. E. Projector augmented-wave method. *Phys. Rev. B: Condens. Matter Mater. Phys.* **1994**, *50* (24), 17953−17979.
(48) Kresse, G.; Joubert, D. From ultrasoft pseudopotentials to the projector augmented-wave method. *Phys. Rev. B: Condens. Matter Mater. Phys.* **1999**, *59* (3), 1758−1775.
(49) Hammer, B.; Hansen, L. B.; Nørskov, J. K. Improved adsorption energetics within density-functional theory using revised Perdew-Burke-Ernzerhof functionals. *Phys. Rev. B: Condens. Matter Mater. Phys.* **1999**, *59* (11), 7413−7421.
(50) Grimme, S.; Ehrlich, S.; Goerigk, L. Effect of the damping function in dispersion corrected density functional theory. *J. Comput. Chem.* **2011**, *32* (7), 1456−1465.
(51) Henkelman, G.; Jónsson, H. Improved tangent estimate in the nudged elastic band method for finding minimum energy paths and saddle points. *J. Chem. Phys.* **2000**, *113* (22), 9978−9985.
(52) Jonsson, H.; Mills, G.; Jacobsen, K. W., Nudged elastic band method for finding minimum energy paths of transitions. In *Classical and Quantum Dynamics in Condensed Phase Simulations*; World Scientific: 1998; pp 385−404.
(53) Henkelman, G.; Jónsson, H. A dimer method for finding saddle points on high dimensional potential surfaces using only first derivatives. *J. Chem. Phys.* **1999**, *111* (15), 7010−7022.
(54) Baerlocher, C.; McCusker, L. B. Database of Zeolite Structures. http://www.iza-structure.org/databases (accessed 12/01/2018).
(55) Newsam, J. M.; Treacy, M. M. J.; Koetsier, W. T.; Gruyter, C. B. D.; Thomas John, M. Structural characterization of zeolite beta. *Proceedings of the Royal Society of London. A. Mathematical and Physical Sciences* **1988**, *420* (1859), 375−405.
(56) Lobo, R. F.; Pan, M.; Chan, I.; Li, H.-X.; Medrud, R. C.; Zones, S. I.; Crozier, P. A.; Davis, M. E. SSZ-26 and SSZ-33: Two Molecular Sieves with Intersecting 10- and 12-Ring Pores. *Science* **1993**, *262* (5139), 1543.
(57) Mathew, K.; Hennig, R. G., Implicit self-consistent description of electrolyte in plane-wave density-functional theory. *eprint arXiv* **2016**, 1601.03346.
(58) Mathew, K.; Sundararaman, R.; Letchworth-Weaver, K.; Arias, T. A.; Hennig, R. G. Implicit solvation model for density-functional study of nanocrystal surfaces and reaction pathways. *J. Chem. Phys.* **2014**, *140* (8), No. 084106.
(59) Rossmeisl, J.; Nørskov, J. K.; Taylor, C. D.; Janik, M. J.; Neurock, M. Calculated Phase Diagrams for the Electrochemical Oxidation and Reduction of Water over Pt(111). *J. Phys. Chem. B* **2006**, *110* (43), 21833−21839.
(60) Mei, D.; Lercher, J. A. Effects of Local Water Concentrations on Cyclohexanol Dehydration in H-BEA Zeolites. *J. Phys. Chem. C* **2019**, *123* (41), 25255−25266.
(61) Hintermeier, P. H.; Eckstein, S.; Mei, D.; Olarte, M. V.; Camaioni, D. M.; Baráth, E.; Lercher, J. A. Hydronium-Ion-Catalyzed Elimination Pathways of Substituted Cyclohexanols in Zeolite H-ZSM5. *ACS Catal.* **2017**, *7* (11), 7822−7829.
(62) McQuarrie, D. A. *Statistical Mechanics*; University Science Books: Sausalito, CA, 2000.
(63) Lanzafame, P.; Papanikolaou, G.; Perathoner, S.; Centi, G.; Migliori, M.; Catizzone, E.; Aloise, A.; Giordano, G. Direct versus acetalization routes in the reaction network of catalytic HMF etherification. *Catal. Sci. Technol.* **2018**, *8* (5), 1304−1313.
(64) Tsilomelekis, G.; Orella, M. J.; Lin, Z.; Cheng, Z.; Zheng, W.; Nikolakis, V.; Vlachos, D. G. Molecular structure, morphology and growth mechanisms and rates of 5-hydroxymethyl furfural (HMF) derived humins. *Green Chem.* **2016**, *18* (7), 1983−1993.
(65) Patil, S. K. R.; Heltzel, J.; Lund, C. R. F. Comparison of Structural Features of Humins Formed Catalytically from Glucose, Fructose, and 5-Hydroxymethylfurfuraldehyde. *Energy Fuels* **2012**, *26*, 5281−5293.
(66) Patil, S. K. R.; Lund, C. R. F. Formation and Growth of Humins via Aldol Addition and Condensation during Acid-Catalyzed Conversion of 5-Hydroxymethylfurfural. *Energy Fuels* **2011**, *25*, 4745−4755.
(67) Mellmer, M. A.; Gallo, J. M. R.; Martin Alonso, D.; Dumesic, J. A. Selective Production of Levulinic Acid from Furfuryl Alcohol in THF Solvent Systems over H-ZSM-5. *ACS Catal.* **2015**, *5* (6), 3354−3359.
(68) Semelsberger, T. A.; Ott, K. C.; Borup, R. L.; Greene, H. L. Role of acidity on the hydrolysis of dimethyl ether (DME) to methanol. *Appl. Catal., B* **2005**, *61* (3), 281−287.
(69) Wan, S.; Waters, C.; Stevens, A.; Gumidyala, A.; Jentoft, R.; Lobban, L.; Resasco, D.; Mallinson, R.; Crossley, S. Decoupling HZSM-5 Catalyst Activity from Deactivation during Upgrading of Pyrolysis Oil Vapors. *ChemSusChem* **2015**, *8* (3), 552−559.
(70) Hulea, V.; Huguet, E.; Cammarano, C.; Lacarriere, A.; Durand, R.; Leroi, C.; Cadours, R.; Coq, B. Conversion of methyl mercaptan and methanol to hydrocarbons over solid acid catalysts − A comparative study. *Appl. Catal., B* **2014**, *144*, 547−553.
(71) Madon, R. J.; Boudart, M. Experimental criterion for the absence of artifacts in the measurement of rates of heterogeneous catalytic reactions. *Ind. Eng. Chem. Fundam.* **1982**, *21* (4), 438−447.
(72) Vannice, M. A. *Kinetics of Catalytic Reactions*; Springer: New York, NY, 2005.
(73) Frillette, V. J.; Haag, W. O.; Lago, R. M. Catalysis by crystalline aluminosilicates: Characterization of intermediate pore-size zeolites by the "Constraint Index. *J. Catal.* **1981**, *67* (1), 218−222.
(74) Jae, J.; Tompsett, G. A.; Foster, A. J.; Hammond, K. D.; Auerbach, S. M.; Lobo, R. F.; Huber, G. W. Investigation into the shape selectivity of zeolite catalysts for biomass conversion. *J. Catal.* **2011**, *279* (2), 257−268.
(75) First, E. L.; Gounaris, C. E.; Wei, J.; Floudas, C. A. Computational characterization of zeolite porous networks: an automated approach. *Phys. Chem. Chem. Phys.* **2011**, *13* (38), 17339−17358.
(76) Madon, R. J.; Iglesia, E. Catalytic reaction rates in thermodynamically non-ideal systems. *J. Mol. Catal. A: Chem.* **2000**, *163* (1−2), 189−204.
(77) Smith, J. M.; Van Ness, H. C.; Abbott, M. M. *Introduction to Chemical Engineering Thermodynamics*, 7th ed.; McGraw-Hill: New York, NY, 2005.
(78) Hansen, H. K.; Rasmussen, P.; Fredenslund, A.; Schiller, M.; Gmehling, J. Vapor-Liquid Equilibria by UNIFAC Group Contribution. 5. Revision and Extension. *Ind. Eng. Chem. Res.* **1991**, *30* (10), 2352−2355.
(79) DeLuca, M.; Kravchenko, P.; Hoffman, A.; Hibbitts, D. Mechanism and Kinetics of Methylating C6−C12 Methylbenzenes with Methanol and Dimethyl Ether in H-MFI Zeolites. *ACS Catal.* **2019**, *9* (7), 6444−6460.
(80) Di Iorio, J. R.; Hoffman, A. J.; Nimlos, C. T.; Nystrom, S.; Hibbitts, D.; Gounder, R. Mechanistic origins of the high-pressure inhibition of methanol dehydration rates in small-pore acidic zeolites. *J. Catal.* **2019**, *380*, 161.
(81) Jones, A. J.; Iglesia, E. Kinetic, Spectroscopic, and Theoretical Assessment of Associative and Dissociative Methanol Dehydration Routes in Zeolites. *Angew. Chem., Int. Ed.* **2014**, *53* (45), 12177−12181.

https://dx.doi.org/10.1021/acscatal.0c01328
ACS Catal. 2020, 10, 6771−6785

(82) Moses, P. G.; Nørskov, J. K. Methanol to Dimethyl Ether over ZSM-22: A Periodic Density Functional Theory Study. *ACS Catal.* **2013**, *3* (4), 735−745.
(83) Ghorbanpour, A.; Rimer, J. D.; Grabow, L. C. Computational Assessment of the Dominant Factors Governing the Mechanism of Methanol Dehydration over H-ZSM-5 with Heterogeneous Aluminum Distribution. *ACS Catal.* **2016**, *6* (4), 2287−2298.
(84) Deshlahra, P.; Carr, R. T.; Iglesia, E. Ionic and Covalent Stabilization of Intermediates and Transition States in Catalysis by Solid Acids. *J. Am. Chem. Soc.* **2014**, *136* (43), 15229−15247.
(85) Denbigh, K. *The Principles of Chemical Equilibrium*, 3rd ed.; Cambridge University Press: New York, NY, 1971.
(86) Yaws, C. L. *Chemical Properties Handbook*; McGraw-Hill: New York, NY, 1999.
(87) Farberow, C. A.; Dumesic, J. A.; Mavrikakis, M. Density Functional Theory Calculations and Analysis of Reaction Pathways for Reduction of Nitric Oxide by Hydrogen on Pt(111). *ACS Catal.* **2014**, *4* (10), 3307−3319.
(88) Bhan, A.; Iglesia, E. A Link between Reactivity and Local Structure in Acid Catalysis on Zeolites. *Acc. Chem. Res.* **2008**, *41* (4), 559−567.
(89) Gounder, R.; Iglesia, E. Catalytic Consequences of Spatial Constraints and Acid Site Location for Monomolecular Alkane Activation on Zeolites. *J. Am. Chem. Soc.* **2009**, *131* (5), 1958−1971.
(90) Jones, A. J.; Zones, S. I.; Iglesia, E. Implications of Transition State Confinement within Small Voids for Acid Catalysis. *J. Phys. Chem. C* **2014**, *118* (31), 17787−17800.
(91) Gounder, R.; Iglesia, E. The catalytic diversity of zeolites: confinement and solvation effects within voids of molecular dimensions. *Chem. Commun.* **2013**, *49* (34), 3491−3509.
(92) Sastre, G.; Corma, A. The confinement effect in zeolites. *J. Mol. Catal. A: Chem.* **2009**, *305* (1), 3−7.
(93) Li, C.; Vidal-Moya, A.; Miguel, P. J.; Dedecek, J.; Boronat, M.; Corma, A. Selective Introduction of Acid Sites in Different Confined Positions in ZSM-5 and Its Catalytic Implications. *ACS Catal.* **2018**, *8* (8), 7688−7697.
(94) Bučko, T.; Hafner, J. The role of spatial constraints and entropy in the adsorption and transformation of hydrocarbons catalyzed by zeolites. *J. Catal.* **2015**, *329*, 32−48.
(95) Gallego, E. M.; Paris, C.; Cantín, Á.; Moliner, M.; Corma, A. Conceptual similarities between zeolites and artificial enzymes. *Chemical Science* **2019**, *10* (34), 8009−8015.
(96) Gallego, E. M.; Portilla, M. T.; Paris, C.; León-Escamilla, A.; Boronat, M.; Moliner, M.; Corma, A. Ab initio" synthesis of zeolites for preestablished catalytic reactions. *Science* **2017**, *355* (6329), 1051.
(97) Baerlocher, C.; McCusker, L. B.; Olson, D. H.; Baerlocher, C.; Burton, A. W.; Baur, W. H.; Broach, R. W.; Dorset, D. L.; Fischer, R. X.; Gies, H.; Kirchner, R. M.; Lobo, R. F.; McCusker, L. B.; Meier, W. M.; Morris, R. E.; Mortier, W. J.; O'Keeffe, M.; Olson, D. H.; Treacy, M. M. J.; van Koningsveld, H.; Terasaki, O. *Atlas of Zeolite Framework Types*, 6th ed.; Elsevier Science: Amsterdam, 2007.

NOTE ADDED AFTER ASAP PUBLICATION

This paper originally published ASAP on June 4, 2020. Due to a production error, an incorrect Supporting Information file was upload. The correct version was reposted on June 4, 2020.

https://dx.doi.org/10.1021/acscatal.0c01328
ACS Catal. 2020, 10, 6771−6785